Response of curved premixed flames to single-frequency and wideband acoustic waves

Hemdan Shalaby [a,*], Kai H. Luo [a], Dominique Thévenin [b]

[a] Department of Mechanical Engineering, University College London, London WC1E 7JE, United Kingdom
[b] Lab. of Fluid Dynamics and Technical Flows, University of Magdeburg "Otto von Guericke", Universitätsplatz 2, D-39106 Magdeburg, Germany

ABSTRACT

The dynamic response of a premixed curved flame interacting with sinusoidal acoustic waves has been numerically studied in the present work. Flame/acoustic interactions are particularly important both from a theoretical point of view and for practical purposes, as a possible trigger mechanism for combustion instabilities. Flames found in practical devices show a complex geometry, far from the planar configuration usually considered in theoretical studies. The particular purpose of the current study is to assess quantitatively the effects of acoustic waves on curved premixed flames, considering both single and wideband frequencies in order to mimic the conditions encountered in practical systems. The interaction process is studied by using Direct Numerical Simulation (DNS) including detailed physicochemical processes and differential molecular diffusion. The chemical reactions are modeled by a 25-step skeletal scheme involving 16 species to describe methane oxidation. The numerical results show strong flame front oscillations back and forth during interaction of the wave with the curved premixed flame. Moreover, the results demonstrate that a single-frequency acoustic wave has a magnifying effect on the preexisting wrinkling of the flame. This extending flame front leads to increasing fuel consumption rate. The effect is found to be maximum at an intermediate excitation frequency of 500 Hz. Interestingly, a wideband excitation from 100 to 1000 Hz leads to significant flame oscillation and the fuel consumption rate is highly increased in that case. As a whole, this study shows that curved flames are much more sensitive to acoustic excitations compared to planar flames, due to the baroclinic torque in combination with other inherent instabilities. An oblique acoustic wave has a similar but slightly enhanced disturbance to the premixed flame. Moreover, non-unity Lewis numbers have significant effects on curved flame-acoustic interaction, even in the present stoichiometric methane flame. However, it presented highly sensitive to the interaction.

1. Introduction

In practical applications, curved flames are the rule and planar flames the exception. This is also true even in simple configurations used for most fundamental studies. A simple premixed flame in a closed tube is a good example of the spontaneous formation of a curved flame due to various modes of instabilities [1–5]. One of the striking phenomena observed under such conditions is the well-known "tulip flame". Curved flames with a shape close to a tulip are found to be fully developed when taking into consideration flame-hydrodynamic interactions [6].

Curved flames of direct relevance for flame-acoustic interactions have been encountered for instance in the experiments by Searby [7], Searby and Rochwerger [8] and then explained analytically by Bychkov [9]. These studies have highlighted two key, competing effects for flame-acoustic interaction: (i) stabilization of the flame instabilities by acoustic waves of moderate amplitudes and (ii) excitation of the parametric instability at the flame front at higher acoustic amplitudes. Later experimental and theoretical works by Aldredge and Killingsworth [10] and Yáñez et al. [11] have built on top of these results. Violent folding of a flame front due to flame-acoustic resonance has been also predicted, obtained and studied by Bychkov [12] and Petchenko et al. [13,14]. Such a resonance may be responsible for the acoustic flame turbulization observed by Searby [7] or Aldredge and Killingsworth [10]. A review concerning premixed flames interacting with acoustic waves can be found in [15].

As a precious complement to experimental studies, Direct Numerical Simulations (DNS) combined with accurate physico-chemical models have been successfully used to study flame-acoustic interaction for premixed [16–18] as well as nonpremixed [19] flames, using different fuels (hydrogen [16,17,19] and syngas [18]). Such studies have delivered essential information to understand the coupling between turbulent flames and acoustic waves [20,21].

Teerling et al. [23] investigated numerically the response of slightly corrugated premixed flames to oscillatory pressure waves using single-step chemistry and unity Lewis number. They observed that the pressure waves can magnify the flame wrinkle due to the Rayleigh–Taylor instability. The present study is intended as an extension of the work by Teerling et al. [23], using more complex physicochemical models in addition to non-unity Lewis number in a DNS. It is important to check if the previous observations would be modified in that case, and how the curved flame will respond quantitatively to single and wideband acoustic waves. In order to isolate the acoustic effects, we study in the present work a curved flame interacting with acoustic waves in an open domain, avoiding any possible influence of solid walls. This interesting aspect of wall influence, obviously encountered in practical applications, will be the subject of future work. The DNS results can in particular be used to answer following questions:

- What is the qualitative response of the curved flame to single and wideband acoustic waves?
- What is the effect of the acoustic wave amplitudes on fuel consumption rate?
- What is the difference between the curved and planar flames with respect to the acoustic energy enhancement?
- What is the effect of an oblique acoustic wave compared with a planar wave disturbance on the curved flame?
- What is the effect of non-uniform Lewis number compared with unity Lewis number?

The rest of the paper is arranged as follows. The mathematical equations are presented in Section 2, followed by a description of the essential computational parameters in Section 3. The outcomes are shown and discussed in Section 4, before the conclusions are drawn.

2. Mathematical equations

In the present work, the employed DNS code is the parallel flame solver, *ParComb* [24–26], which solves the full compressible reactive Navier–Stokes system coupled with detailed chemistry and multicomponent transport models via coupling with the *chemkin* [27], *transport* [28] and *eglib* [29] libraries. Using classical notations [30–32] and ignoring all external forces, the conservation equations solved in *ParComb* are as follows:

Mass conservation

$$\frac{\partial \rho}{\partial t} + \frac{\partial (\rho u_j)}{\partial x_j} = 0 \qquad (1)$$

Momentum conservation

$$\frac{\partial (\rho u_i)}{\partial t} + \frac{\partial (\rho u_j u_i)}{\partial x_j} = -\frac{\partial p}{\partial x_i} + \frac{\partial \tau_{ij}}{\partial x_j}; \qquad i = 1, 2, 3 \qquad (2)$$

Species balance

$$\frac{\partial (\rho Y_k)}{\partial t} + \frac{\partial [\rho(u_j + V_{kj})Y_k]}{\partial x_j} = \dot{\omega}_k; \quad k = 1, N_s \qquad (3)$$

Energy conservation

$$\frac{\partial (\rho e_t)}{\partial t} + \frac{\partial [(\rho e_t + p)u_j]}{\partial x_j} = -\frac{\partial q_j}{\partial x_j} + \frac{\partial (\tau_{ij}u_i)}{\partial x_i} \qquad (4)$$

Ideal gas law

$$\frac{p}{\rho} = \frac{R}{\overline{W}} T \qquad (5)$$

where ρ denotes mixture density, u_j the components of the hydrodynamic velocity, p the pressure, τ_{ij} the stress tensor, N_s the total number of species, V_{kj} the component of the diffusion velocity of species k in the direction j, $\dot{\omega}_k$ the chemical production rate of species k and q_j the jth-component of the heat flux vector.

The above system of governing equations, together with considered thermodynamical relations (e.g., the ideal gas law), chemistry and transport models described later are solved on a three-dimensional Cartesian grid with high-order numerical schemes. A sixth-order central scheme progressively reduced to a one-sided fourth-order scheme near the boundaries is used for spatial discretization. The improved skew-symmetric formulation [33] has been implemented for the convective terms in order to reduce numerical dissipation and increase stability. According to this scheme, the derivative of a general convective term can be written as:

$$\frac{\partial (\rho a u_j)}{\partial x_j} = \frac{1}{2} \frac{\partial (\rho a u_j)}{\partial x_j} + \frac{1}{2} \frac{a \partial (\rho u_j)}{\partial x_j} + \frac{\rho u_j}{2} \frac{\partial a}{\partial x_j} \qquad (6)$$

Time integration is performed in an explicit manner with a fourth-order Runge–Kutta scheme, as implicit methods do not seem to be beneficial for the specific problems considered [34] and are difficult to parallelize efficiently. A Courant–Friedrichs–Levy (CFL) condition for the convective terms and a Fourier condition pertaining to the diffusion terms are treated to ensure the stability of the explicit integration and determine a suitable time-step. Boundary conditions are treated with the help of the Navier–Stokes Characteristic Boundary Condition (NSCBC) technique [41], extended to take into account multicomponent thermodynamic properties [35].

2.1. Chemistry

The resulting reaction rate comprising N_s species with an arbitrary number of elementary reactions N_r for reaction j is then the difference between the forward and backward rates, given (without third bodies) by

$$r_j = k_{fj} \prod_{i=1}^{N_s} n_i^{v'_{ij}} - k_{bj} \prod_{i=1}^{N_s} n_i^{v''_{ij}}, \qquad j \in [1, N_r] \qquad (7)$$

where $n_i = \rho Y_i / M_i$ denotes the molar concentration of species i with k_{fj} and k_{bj} are respectively, while v'_{ij} and v''_{ij} are the forward and backward stoichiometric coefficient of the ith species in the jth reaction, classically expressed via the Arrhenius law [36]:

$$k = AT^\beta \exp\left(-\frac{E_a}{RT}\right) \qquad (8)$$

The parameters A and β of the pre-exponential factor and the activation energy E_a are determined experimentally [36,37]. The two reaction constants are linked using the equilibrium constant $k_{j,eq}(p,T) = k_{fj}/k_{bj}$ which is suitably defined by the thermodynamic properties of the chemical components involved in the reaction.

Finally, the molar production rate of species i is given by taking the sum of all contributions from the elementary reactions:

$$\dot{w}_i = M_i \sum_{j=1}^{N_r} v_{ij} r_j, \qquad i \in [1, N_s] \qquad (9)$$
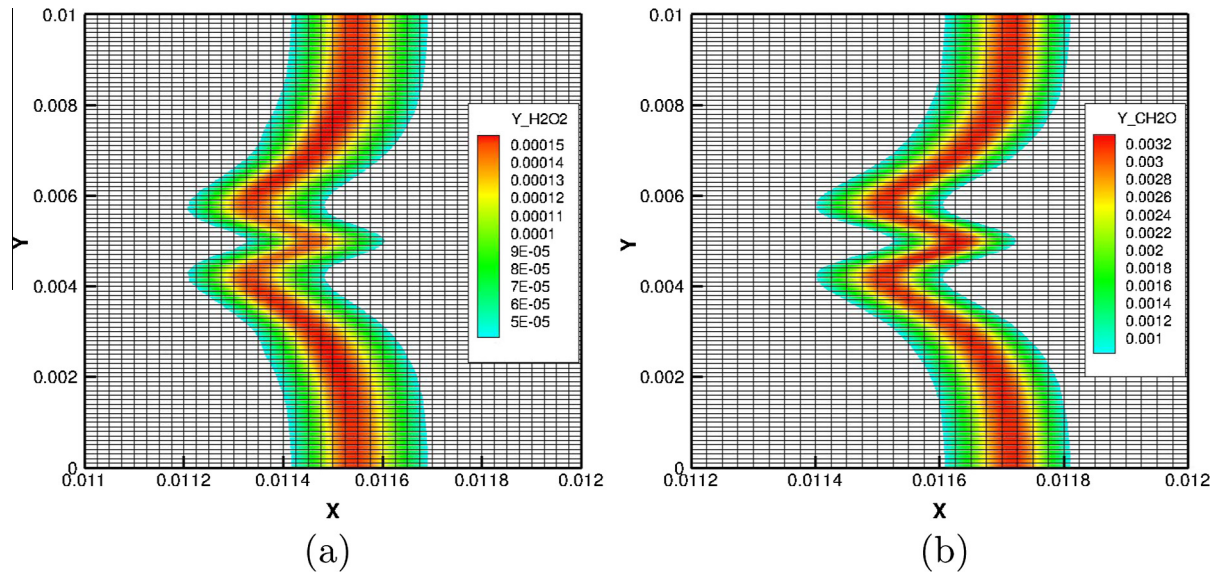
where $v_{ij} = v'_{ij} - v''_{ij}$.

Fig. 1. Example of instantaneous mass fraction of H₂O₂ and CH₂O, showing the grid resolution for these stiff species.

2.2. Molecular diffusion

In addition to chemistry, detailed models are also employed for the computation of the diffusive processes. Neglecting the Dufour effect, the diffusion velocity of species i in the mixture is expressed as

$$\mathbf{V}_i = -\sum_{k=1}^{N_s} D_{ik}\mathbf{d}_k - D_i^T \frac{\nabla T}{T} \tag{10}$$

where D_{ik} is the multi-species diffusion coefficient of species i into species k and depends on all state variables. This diffusion matrix is symmetric, i.e., $D_{ik} = D_{ki}$ and the mass conservation constraint associated with the species diffusion velocities reads $\sum_{i=1}^{N_s} Y_i\mathbf{V}_i = 0$. The species diffusion driving force $\mathbf{d}_k$ is a vector that takes into account gradients of mole fraction and pressure. In most cases, as in our work, the pressure-induced diffusion is neglected and the external forces $\mathbf{f}_j$ are considered to act identically on all species, resulting simply to $\mathbf{d}_k = \nabla X_k$. D_i^T is the thermal diffusion coefficient of species i while the combined term $D_i^T \nabla T/T$ is the so-called Soret or thermo-diffusion effect, which accounts for the diffusion of mass due to temperature gradients [32,38].

Here, we consider the Hirschfelder–Curtiss approach [39], whereby an approximate diffusion coefficient, D_i^* for the species i is given as

$$D_i^* = \frac{(1 - Y_i)}{\sum_{k=1,k\neq i}^{N_s}(X_k/D_{ik})} \tag{11}$$

where X_k is the mole fraction of species k. It is equivalent to keeping only the first term of the series expansion of the diffusion matrix [32]. Here, for mass to be conserved, the diffusion velocity $\mathbf{V}_i$ for species i is divided into a predictor ($\mathbf{V}_i^*$) and a corrector ($\mathbf{V}_c$) term:

$$\mathbf{V}_i = \mathbf{V}_i^* + \mathbf{V}_c; \qquad \mathbf{V}_i^* = -D_i^* \frac{\nabla X_i}{X_i}; \qquad \mathbf{V}_c = -\sum_{k=1}^{N_s} Y_k\mathbf{V}_k^* \tag{12}$$

A further discussion of this topic can be found in [40]

3. Computational parameters

All simulations analyzed in this work have been carried out with the DNS code *ParComb* already employed in several previous studies of flame/acoustic interaction [16,18–21]. It is a finite-difference

DNS code solving the compressible Navier–Stokes equations for multicomponent reacting flows. The chemical reaction mechanism originally proposed in [42] and involving a 25-step skeletal scheme with 16 species has been used to describe methane oxidation. The computational domain is a box of length 2.0 cm in x-direction and 1.0 cm in y-direction with a fixed spatial resolution of 25 μm as shown in Fig. 1, necessary to resolve correctly not only the smallest flow structures but also stiff species, in particular CH₂O or H₂O₂. The typical time step used in our computations is 20 ns The left-hand boundary condition is a subsonic inlet with imposed acoustic pressure, while the right-hand boundary condition is a non-reflecting subsonic outlet as shown in Fig. 2. Top and bottom boundaries are periodic. The x-direction is the main direction of propagation for the flame (spontaneously from right to left, i.e., from burnt gas towards fresh gas), as well as for the acoustic wave (initiated at the left boundary of the domain within the fresh gas, and propagating towards the right direction).

The initial profile of a stoichiometric curved premixed methane flame has been constructed by extending an initially 1D premixed laminar flame in x-direction to lateral directions. The curvature is introduced by a sech-function so that the curved flame resembles a typical tulip flame observed in experiments. However, the following 1D profile is considered:

$$\phi(x) = \phi_0 + \frac{A}{2}\left(1 + \tanh\left[B\left(x - \frac{1}{7}(3X_{min} + 4X_{max})\right)\right]\right) \tag{13}$$
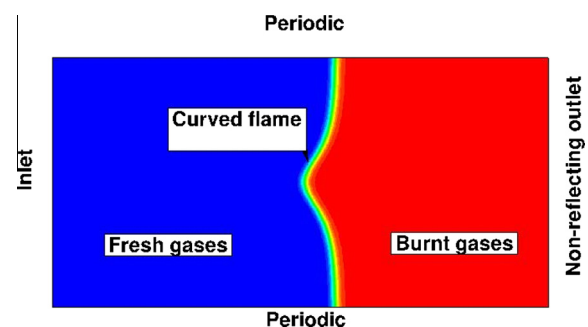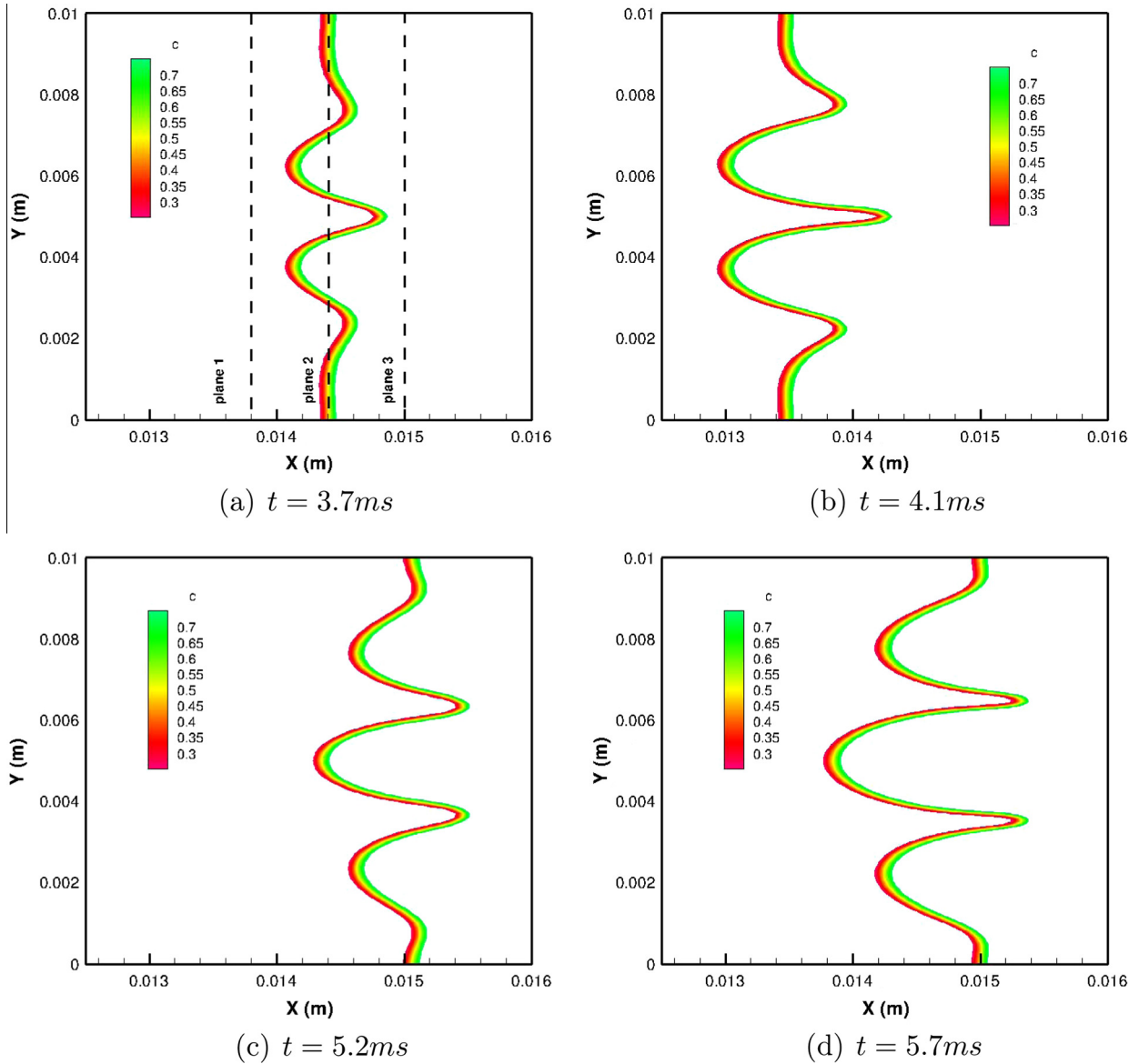

Fig. 2. Representation of the flame configurations and initialization.

(a) $t = 3.7ms$

(b) $t = 4.1ms$

(c) $t = 5.2ms$

(d) $t = 5.7ms$

Fig. 3. Evolution of the flame front (zoom on the flame region) represented by the reaction progress variable c when interacting with the tenth period of an acoustic wave at a frequency of 700 Hz for a pressure amplitude of 1000 Pa.

on the domain $x\epsilon[X_{min}, X_{max}]$. Where, A denotes ϕ difference between burned and fresh gases mixture. Parameter B determines the stiffness of the initial profile. Then to extend it to a flat 2D profile, T2DFLAT function is considered as a function of two variables x and y as $T2DFLAT(x,y) = \phi(x)$. So, for each value of y, we have the same evolution in x. In case of curved flame, the same profile of 1D has been considered but the way to extend to 2D is changed as $T2DCURVE(x,y) = \phi(x + f(y))$, where $f(y)$, with $y\epsilon[Y_{min}, Y_{max}]$ is given by:

$$f(y) = \frac{\mid Y_{max} - Y_{min} \mid}{D} sech\left(\frac{C(y - \frac{Y_{min}+Y_{max}}{2})}{\mid Y_{max} - Y_{min} \mid}\right) \qquad (14)$$

where the parameter D is related to the height of the bump and C is related to the spreading of the bump. In our case, $D = 8$ and $C = 10$ have been chosen.

For a quantitative analysis it is useful to introduce a few classical parameters. The speed of sound in the fresh gas region is written as $\bar{c}$, and the domain length in x-direction is l_x. The order of magnitude of the interaction time of the flame with a single,

isolated acoustic wave is then simply $t_{int} = l_x/\bar{c}$. The imposed acoustic pressure is defined as a sinusoidal wave as follows

$$p' = p_0 + Asin(\omega(t - t_0)) \qquad (15)$$

where A denotes the pressure amplitude, p_0 the initial pressure, t the time, t_0 the initial time of the imposing acoustic pressure, and $\omega = 2\pi f$ with the frequency f.

For the case considered in the present paper the acoustic wave typically involves $n \succ 10$ periods. The pressure wavelength is much larger than the mean flame thickness.
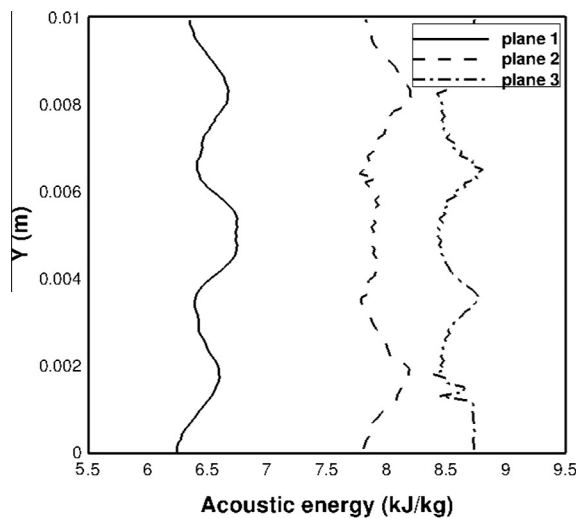
4. Results and discussions

DNS results were obtained for a curved flame, on which oscillatory acoustic disturbances at fixed frequencies of 200, 500, 700, and 1000 Hz were imposed. In a second step, a wideband frequency range from 100 to 1000 Hz was imposed instead. For both configurations, increasing wave amplitudes of 500, 800, and 1000 Pa have been considered. All these acoustic disturbances
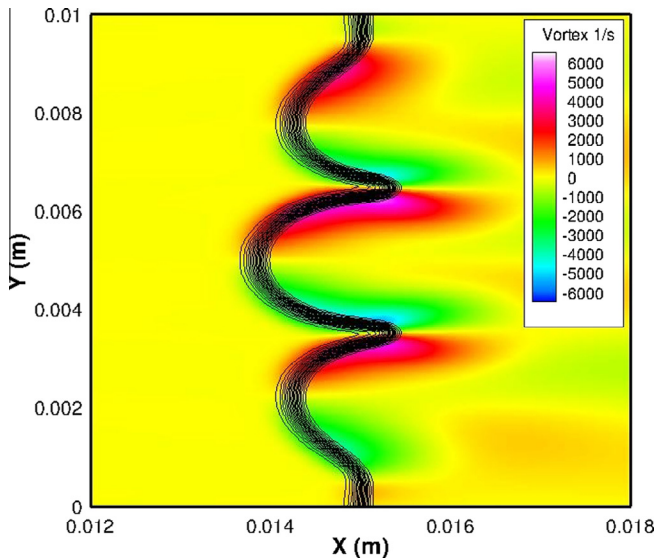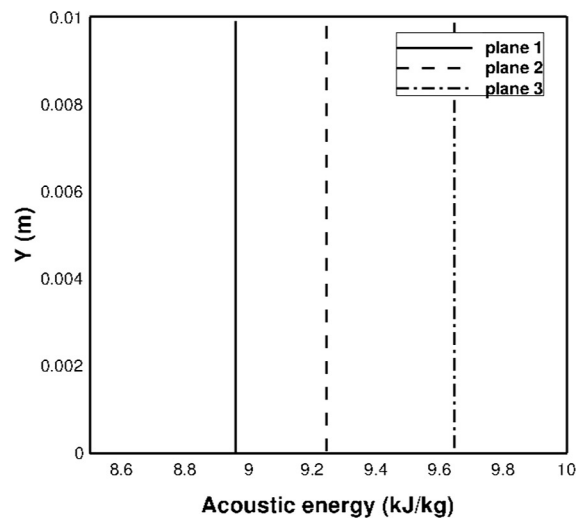
Fig. 4. Development of vortex pairs in the hot gas region after interaction of the acoustic wave with the curved flame (frequency of 700 Hz, amplitude of 1000 Pa, same conditions as for Fig. 3). Continuous solid lines represent isolevels of reaction progress variable, while the color map shows vorticity.

Fig. 6. Fuel consumption rate in the numerical domain as a function of time during flame-acoustic interactions. Shown are the results for single-frequency waves (at 200, 500, 700, and 1000 Hz) as well as wideband wave, all at an amplitude of 1000 Pa. For comparison, the evolution of the curved flame without any acoustic excitation is shown as well.

were initialized at the left boundary of the DNS domain and advance to the right through the fresh gas in a direction mostly normal to the initially curved flame. The temporal evolution of the flame front interacting with the tenth period of a single-frequency acoustic wave is shown in Fig. 3 for a frequency of 700 Hz. Here, the flame front is represented by the progress variable c, derived from the temperature as $(T - T_f)/(T_b - T_f)$, where T_f and T_b are the fresh and burned gas temperatures. It can be seen that the flame front is intensely stretched and curved during the interaction. The relative increase in flame surface area due to the interaction with the acoustic wave is very strong, up to 30% during this cycle. During each period of the interaction, the flame front oscillates back and forth with a large amplitude, as can be seen from Fig. 3. For the cycle presented here, this global flame movement corresponds to about 20 times the thermal flame thickness.

Interestingly, such a strong flame oscillation had never been observed in our previous studies when starting from a globally planar flame, but is strongly reminiscent of experimental results described in [43] and in the references discussed in this review article. It is well known that instabilities of type Darrieus–Landau, Rayleigh–Taylor and thermoacoustics may cause flame front wrinkling and cusp formation. However, it is still unclear if any of these instabilities may alone explain the different responses of an initially planar and an initially curved flame to the acoustic perturbation.

Generation of strong vortical structures is observed during the interaction on the hot gas side of the flame, as shown in Fig. 4. This is a consequence of the large baroclinic torque found in this configuration, in competition with the dilatation term found within the
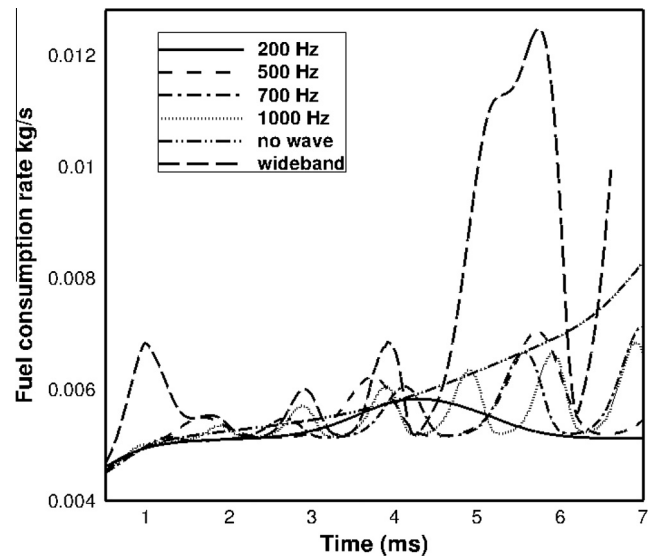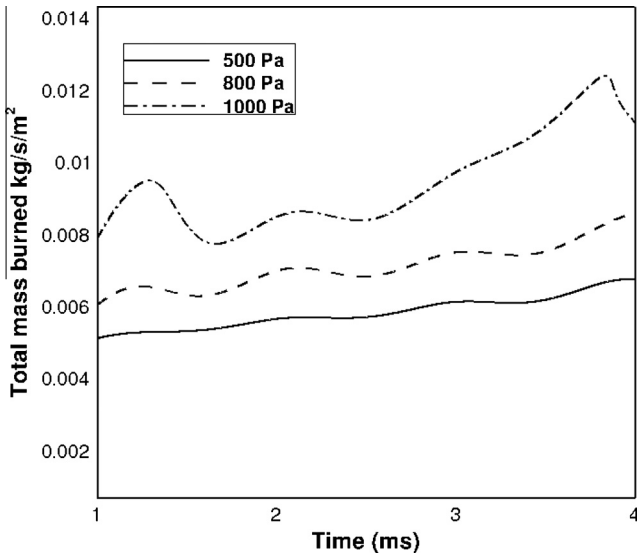

(a)

(b)

Fig. 5. Example of instantaneous acoustic energy in case of initially curved (a) and initially planar (b) flames at three positions (Planes 1, 2 and 3 are shown in Fig. 3(a)). Note the different scales of the horizontal axis.

Fig. 7. Total mass of fuel burned as a function of time for increasing wave amplitude of 500, 800, and 1000 Pa at a single wave frequency of 700 Hz.

Fig. 9. Fuel consumption rate of lower and top points pressure waves as a function of time during flame-acoustic interactions. The results are for a single-frequency wave 700 Hz with an amplitude of 1000 Pa.

flame region. There is a strong misalignment of the pressure gradient and density gradient in the initially curved flame when interacting with the acoustic wave. This leads to an increased baroclinic torque, which in turn leads to strong vorticity generation and to an intensive wrinkling of the flame front. This Taylor instability, which has been already described by many authors (e.g., [44]), is almost absent for an initially planar flame. This observation explains at least partly the different responses of the initially planar and curved flames during interaction with acoustic waves. On the other hand, in a flow that is expanding, dilatation is a positive quantity and the corresponding term leads to a decrease in vorticity magnitude, reducing the induced flame wrinkling. When moving further to the right, the generated vortical structures are rapidly dissipated due to the high viscosity of the hot gases.

Turning now to examining the combustion instabilities in terms of acoustic energy production, three planes in space have been extracted from the computational domain. In what follows, Plane 1 is locate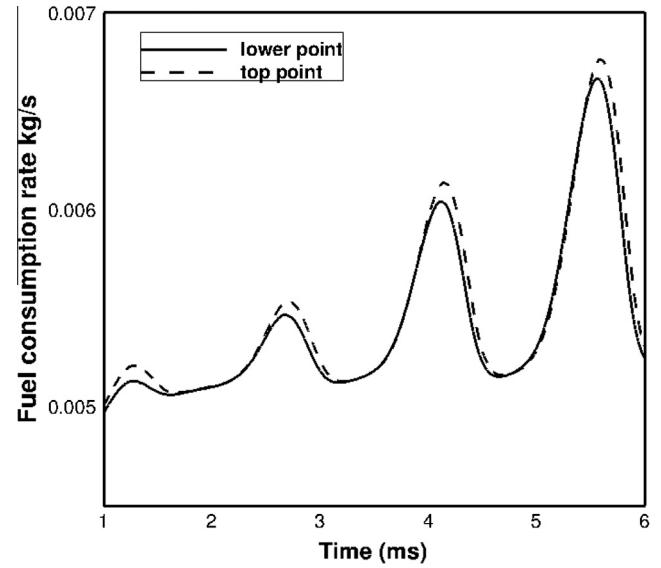d just upstream of the reaction zone; Plane 2 is the average position of the reaction zone; Plane 3 is in the post-reaction zone. All three planes are shown in Fig. 3(a). Now, Fig. 5(a) shows the acoustic energy defined as $\left(\frac{\rho_0 \mathbf{u}_1^2}{2} + \frac{p_1^2}{2\rho_0 c_0^2}\right)$ as derived in [22], where as usual $\mathbf{u}_1$ and p_1 are the fluctuation velocity and pressure, respectively, while quantities with index 0 denote the unperturbed state. As seen in Fig. 5(a) the interaction of the acoustic wave with the initially curved flame leads in average to an increase by about 25% in acoustic energy between Plane 1 and Plane 2, i.e., when entering the active reaction zone. After having completely crossed the flame, the acoustic energy has been further increased by about 12% between Plane 2 and Plane 3. As a whole, the increase in acoustic energy is almost 40%. Considering exactly the same conditions but for an initially planar flame, parallel to the traveling acoustic waves, the increase in acoustic energy occurs again throughout the flame but with a much lower amplitude
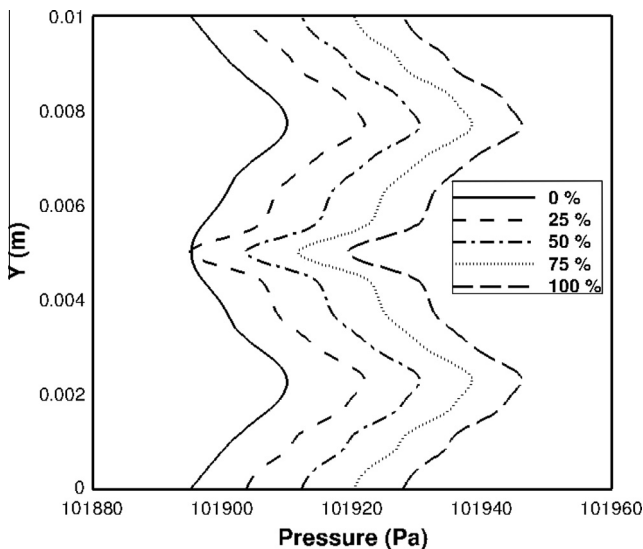

Fig. 8. Oblique pressure waves at inlet boundary with a single wave frequency of 700 Hz and an amplitude of 1000 Pa at $t = 0.2$ ms.
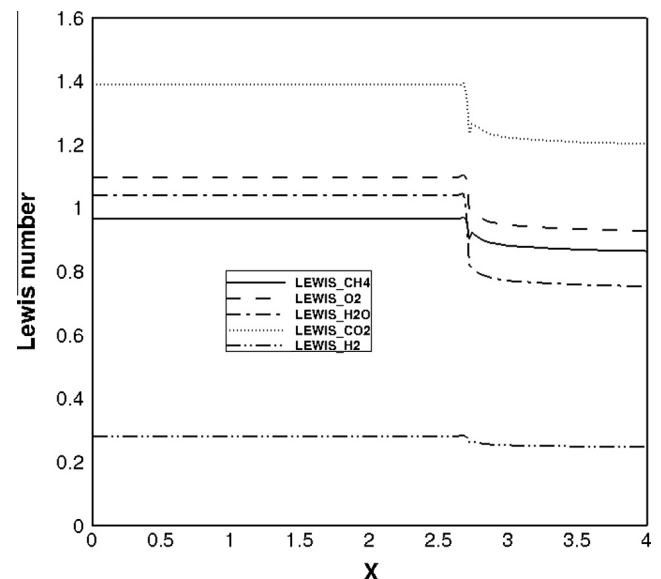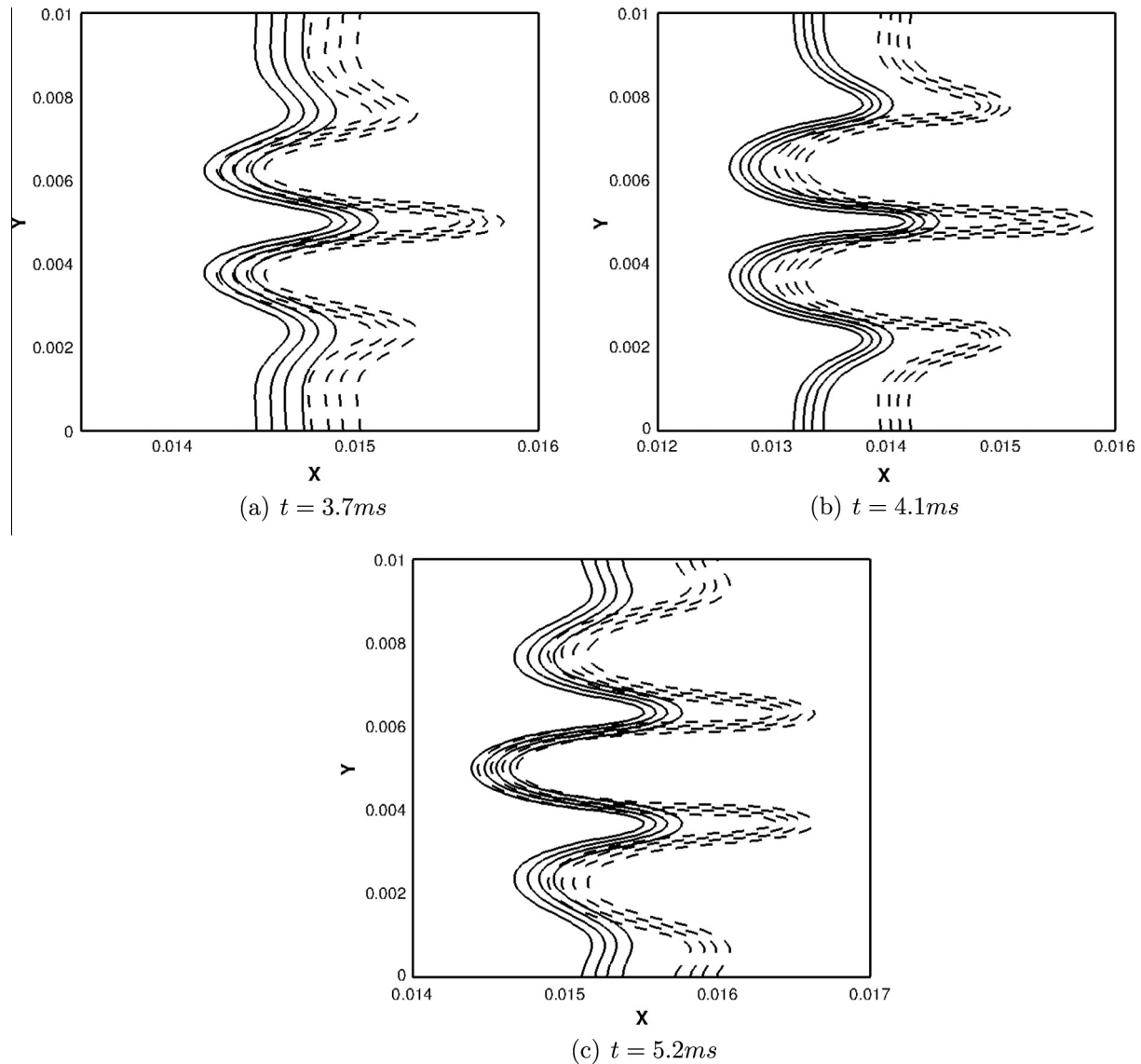

Fig. 10. Variations of Lewis numbers for the main species in a stoichiometric curved premixed methane air flame in the middle of Y direction.

(a) $t = 3.7ms$

(b) $t = 4.1ms$

(c) $t = 5.2ms$

Fig. 11. Instantaneous field of heat release for non-uniform and unity Lewis numbers, respectively. Solid line corresponds to non-uniform and dashed line corresponds to unity Lewis numbers.

(Fig. 5(b)), less than 9%, and mostly in the post-flame region. This is a considerable difference, showing that analyses restricted to planar configurations should be applied with caution to flames with a more complex geometry.

The behavior observed in Fig. 3 is analyzed in the light of flame activity in Fig. 6. The time evolution of the fuel consumption rates shows continuously increasing flame wrinkling during the first cycles, with no evidence of saturation yet. Interestingly, the strongest oscillations in fuel consumption rate are neither found for the lowest (200 Hz) nor for the highest (1000 Hz) frequency, but in the intermediate range, for $f_{ac} = 500$ Hz. For this frequency, the peak fuel reaction rate noticeably exceeds that observed without acoustic excitation during several periods, while the low-frequency case always remains below the unperturbed flame. It is surprising that, the wideband excitation increases extremely rapidly and finally leads to flame destabilization, with a low fuel consumption rate. Prolonging the DNS simulations, a saturation of the oscillations is finally observed, depending on the applied frequency, supporting the findings discussed in [23]. This dynamic equilibrium condition starts around $t = 6.5$ ms at a frequency of 1000 Hz, $t = 8.2$ ms at a frequency of 700 Hz, $t = 9.9$ ms at a frequency of 500 Hz, but is still not achieved at 10 ms (the longest DNS simulation) for a frequency of 200 Hz. After having reached this dynamic equilibrium state, a constant average fuel consumption rate can be computed, averaging over the oscillations. Calculated average values were 6.0 g/s at 1000 Hz, 6.4 g/s at 700 Hz, and 7.0 g/s at 500 Hz, all those values being given for an amplitude of 1000 Pa. A much lower value would probably be obtained at a frequency of 200 Hz, but could only be accurately computed with a much longer simulation.

It is clear that the wideband excitation leads to highly noticeable oscillation of the fuel consumption rate. Since it covers the frequency range between 100 and 1000 Hz, thus encompassing the most active frequency of 500 Hz, strong modifications and oscillations of the flame structure were expected.

The total mass of fuel burned as a function of time is shown in Fig. 7 for increasing pressure amplitude of 500, 800, and 1000 Pa at a single frequency of 700 Hz. It can be deduced from Fig. 7 that the amplitude of the imposed acoustic wave has a significant effect on the total fuel consumption integrated over the full computational domain. An increasing pressure amplitude leads to a roughly proportional increase of the total fuel consumption. This finding is consistent with those discussed by Teerling et al. [23], based on a

quite different approach. They found that the mass burning flux increases initially linearly with the amplitude of the acoustic wave, and also with increasing frequency. While the first observation is directly supported by the present study, the second one appears to hold only up to a certain limit frequency in our case.

Up to now, our analysis was restricted to planar pressure waves which were imposed in a direction perpendicular to the direction in which the initial flame propagates. The question now is: what should be the response of the curved flame to oblique pressure waves? In order to impose oblique pressure waves, time-lag has been defined for different points along the inlet boundary, where the time-lag was computed from the wave propagation speed (speed of sound $\bar{c}$) and the height of the DNS domain in Y-direction: while the lower point is associated with "Time", the middle point is associated with ($Time - 0.5 * Timelag$) and the top point with ($Time - Timelag$), and so on for all intermediate points. By this way, it is sufficient to create oblique pressure waves. Figure 8 shows the oblique pressure waves for lower and top points in addition to intermediate points at $t = 0.2$ ms. It appears that the difference between lower and top point not more than 30 Pa. The question now is: should these small differences in oblique pressure waves lead to any significant increase in the flame surface and hence the mass burning rate?

Figure 9 shows the comparison of a planar pressure wave (lower point) and an oblique pressure wave (top point) in terms of the fuel consumption rate. For an oblique pressure wave imposed to the flame, a slight increase in fuel consumption rate is expected through the effect of the baroclinic torque, because the oblique wave increases the misalignment between the pressure gradient and the density gradient. The enhanced vorticity generation, possibly coupled with the Kelvin–Helmholtz instability, is able to increase the flame surface and hence the fuel consumption rate.

In our present work, non-uniform Lewis numbers in space have been considered. Cuenot and Poinsot [45] concluded that in the case of the fuel and oxidizer Lewis numbers taking any different values, flame properties such as the adiabatic flame temperature were not monotonic functions of the Lewis numbers. However, they only considered a simplified one-step chemistry. Non-uniform Lewis numbers of species in space are expected to affect the position of the flame and the diffusion rate of each species. In some instances, the flame shifts as a result of smaller Lewis number because the amount of fuel at the flame decreases with Lewis number. In the meantime, the diffusion speed has increased leading to a smaller flame temperature. Figure 10 shows variations of the Lewis numbers of main species in the middle of the computational domain through the flame front. This finding is in agreements with Poinsot and Veynante [46] findings which showed a small change of Lewis number through the flame front. Furthermore, they speculated that constant Lewis numbers is usually a reasonable approximation in many flames. The question now is: is using constant or unity Lewis numbers a reasonable simplification in the curved flames under considerations?

Figure 11 represents a comparison between non-uniform and unity Lewis numbers in terms of the instantaneous field of heat release rate. The flame fronts get strongly stretched and curved by interaction with the acoustic waves, leading to considerable modifications of the heat release in both cases. However, the distortion of the flame fronts is much more severe in the unity Lewis number case than in the non-uniform, non-unity Lewis number case at all the time instants. This is because that unity Lewis number means species diffuse as fast as heat. In a real flame with detailed chemistry, different species have different Lewis numbers and the Lewis numbers also vary in space. As a result of the non-coordinated diffusion among the different species, the flame front movement is inhibited.

It is well known that there are Lewis number instabilities as shown in previous work of Edwards et al. [47]. They studied, the development of pressure disturbance to a planar premixed flame front. However, they stated that variations of Lewis number are found to have very little effect on the progress of the flame-acoustic interaction. In a more recent work, Teerling et al. [23], stated that the induced pressure wave was affected by the Lewis number, especially for values much smaller than unity when the inherent instability becomes apparent. In contrast to earlier findings of [47] and recent findings of [23], the present study shows that non-uniform Lewis number in space and non-unity Lewis numbers for species lead to a very significant difference in the predicted total heat release as shown in Fig. 12 with respect to the unity Lewis number case. From Fig. 12, we can see that in the case of non-uniform Lewis number, the total heat release increases by as much as 60% case of unity Lewis number and the heat release rate fluctuation and consequently combustion instability are much stronger. This finding has important implications for developing combustion models based on unity Lewis number, at least for the case of curved flames under imposed pressure perturbations.

This behavior observed in Fig. 3 can now be further clarified by the results in Fig. 13. The time series of mass burning rates show that as combustion instability sets in, the amplitude of reaction rate fluctuations first increases and then reach a almost constant value. In this state, the curved flame and acoustic wave can be considered to be in a dynamic equilibrium, that is, limit cycle oscillations. The starting time of dynamic equilibrium slightly differs for the cases of non-uniform/non-unity and unity Lewis numbers. Figure 13 showed that the dynamic equilibrium was at $t = 7.0$ ms in the case of non-uniform Lewis numbers, and at $t = 8.2$ ms with unity Lewis number. Furthermore, Fig. 13 showed that, when the curved flame and acoustic wave have reached the dynamic equilibrium state, average mass burning rate can be approximated by a straight line, neglecting the small amplitude oscillations. The calculated average values are 7 g/s with the case of non-uniform Lewis numbers, and 8 g/s with unity Lewis number. Finally, the flame oscillations as seen Fig. 3 can be explained as follows. For the premixed flame considered, the location of the flame front is determined by the balance between the propagation speed from the left to the right and the speed of the incoming fresh mixture from the left. When the flame propagation speed increases due to increasing heat release rate as shown in Fig. 13, the flame front
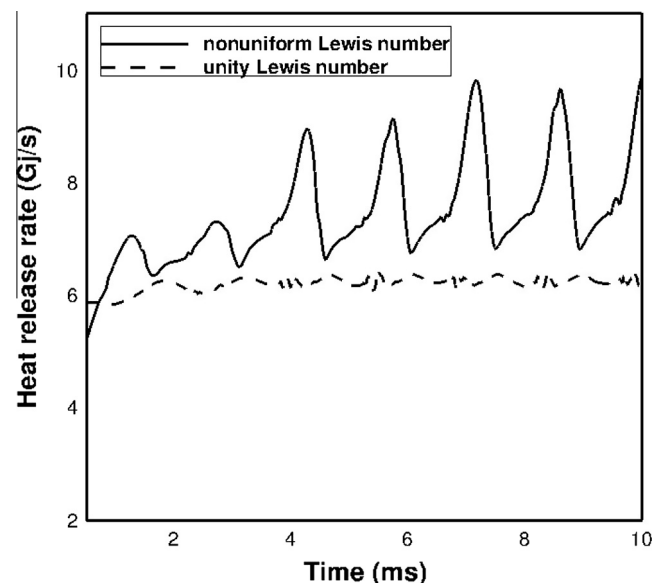

Fig. 12. Temporal evolution of heat release for a non-uniform and a unity Lewis numbers at a pressure amplitude of 1000 Pa with a single frequency of 700 Hz.
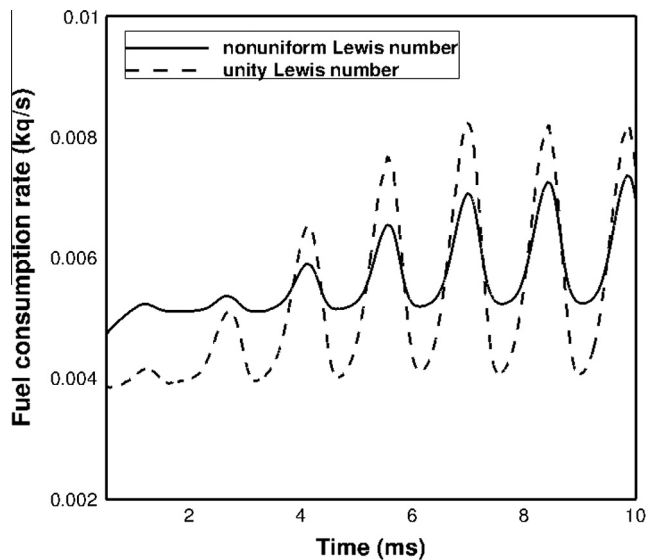
Fig. 13. Mass burning rate, as a function of time a non-uniform and for a unity Lewis numbers at a pressure amplitude of 1000 Pa with a single frequency of 700 Hz.

would move to the left. When the overall heat release rate decreases, the propagation speed would decrease and the flame front would be pushed back from the right to the left. In the meantime, the shape of the flame front changes as a result of the various instabilities.

5. Conclusions and perspectives

The present work was designed to study the effects of acoustic waves on curved premixed flames, building on top of previous analyses dedicated to planar flames. Single frequencies of 200, 500, 700, and 1000 Hz have been considered. Additionally, a wideband excitation covering the range from 100 to 1000 Hz has been implemented as well. Different wave amplitudes have been considered in the simulation.

The DNS results incorporating realistic chemistry and detailed transport model reveal strong flame front oscillations when curved flames are excited by acoustic waves of both a single and wideband frequencies. The same setup but with a planar flame shows no such a flame instability. The difference is attributed to the presence of strong Taylor instability or baroclinic torque in the curved flame, which arises from the misalignment between the pressure gradient and the density gradient at the flame fronts. The resulting vortice generation leads to periodic change in the shape of the flame fronts, such an instability is likely to be coupled with the Rayleigh–Taylor instability and Kelvin–Holmholtz instability to augment the effect. Consequently, the reaction rate fluctuation in a curved flame is much stronger than in a planar flame subjected to an acoustic wave, causing the curved premixed flame front to oscillate back and forth in the axial direction. As a consequence, curved flames appear to be much more sensitive to acoustic excitations than planar flames. In a curved flame, the acoustic energy is increased by about 40% from the fresh gas to the burnt gas sides, compared to less than 9% for the same conditions for a planar flame. When exciting the curved flame with a single frequency, a dynamic equilibrium or limit cycle oscillation establishes after a few cycles, but the equilibrium time depends on the relevant parameters such as the frequency. Excited at 1000 Hz, equilibrium is already reached within less than 7 ms, while more than 10 ms are necessary at 200 Hz. The amplitude of the total fuel consumption increases at first linearly with increasing amplitude of the

acoustic wave. Fuel consumption rate is increased most for a single excitation frequency of 500 Hz, with a lower increase for both higher and lower frequencies. As expected, the wideband excitation leads to more pronounced oscillation in the fuel consumption rate compared with any single frequency. A slight enhancement in flame instability has been observed when an oblique acoustic wave interact with the curved flame compared with a normal acoustic wave, again due to larger baroclinic torque. The curved flame-acoustic interaction has been also affected by the Lewis number effect. The present study considers not only non-unity Lewis numbers for various species but also spatial variations of the Lewis numbers. The latter change rapidly across the flame front. The flame front distortion is more severe in the case of constant, unity Lewis number as compared with the case with non-uniform, non-unity Lewis numbers, where the non-coordinated diffusion of species inhibits the flame front movement. Interestingly, the Lewis numbers also have an influence on the amplitude of the limit cycle oscillations.

A limitation of the present study is that flame-acoustic interaction in only open domain have been considered. It would be interesting to involve wall boundaries as well, as encountered in reality. This will be the subject of future studies.

References

[1] L. Kagan, G. Sivashinsky, Combust. Flame 134 (2003) 389–397.
[2] H. Xiao, Q. Wang, X. He, J. Sun, L.Y. Yao, Int. J Hydrogen Energy 35 (2010) 1367–1376.
[3] S.B. Dorofeev, Proc. Combust. Inst. 33 (2011) 2161–2175.
[4] M. Matalon, Proc. Combust. Inst. 32 (2009) 57–82.
[5] M. Matalon, P. Metzener, J. Fluid Mech. 336 (1997) 331–350.
[6] H. Xiao, Q. Wang, X. He, J. Sun, X. Shen, Int. J Hydrogen Energy 36 (2011) 6325–6336.
[7] G. Searby, Combust. Sci. Technol. 81 (221) (1992) 221–231.
[8] G. Searby, D. Rochwerger, J. Fluid Mech. 231 (1991) 529–543.
[9] V. Bychkov, Phys. Fluids 11 (1999) 3168–3173.
[10] R. Aldredge, N. Killingsworth, Combust. Flame 137 (2004) 178–197.
[11] J. Yáñez, M. Kuznetsov, R. Redlinger, Combust. Flame 160 (2013) 2009–2016.
[12] V. Bychkov, Phys. Rev. Lett. 89 (2002) 168302.
[13] A. Petchenko, V. Bychkov, V. Akkerman, L. Eriksson, Phys. Rev. Lett. 97 (2006) 164501.
[14] A. Petchenko, V. Bychkov, V. Akkerman, L. Eriksson, Combust. Flame 149 (2007) 418–434.
[15] T. Lieuwen, J. Propu. Power 19 (2003) 765–781.
[16] A. Laverdant, D. Thévenin, Combust. Flame 134 (1-2) (2003) 11–19.
[17] A. Laverdant, D. Thévenin, Comptes Rendus de l'Académie des Sciences-Mécanique 333 (2005) 29–37.
[18] H. Shalaby, A. Laverdant, D. Thévenin, in: Twelfth International Congress on Sound and Vibration, Lisbon, Portugal, 2005.
[19] A. Laverdant, L. Gouarin, D. Thévenin, Combust. Theory Modell. 11 (4) (2007) 585–602.
[20] H. Shalaby, A. Laverdant, D. Thévenin, Proc. Comb. Inst. 32 (2009) 1473–1480.
[21] H. Shalaby, A. Laverdant, D. Thévenin, Acta Acustica 95 (2009) 428–439.
[22] F. Nicoud, T. Poinsot, Combust. Flame 142 (2005) 153–159.
[23] O.J. Teerling, A.C. Mcintosh, J. Brindley, V.H. Y Tam, Proc. Comb. Inst. 30 (2005) 1733–1740.
[24] R. Hilbert, F. Tap, H. El-Rabii, D. Thévenin, Prog. Energy Combust. Sci. 30 (2004) 61–117.
[25] R. Hilbert, D. Thévenin, Combust. Flame 128 (2002) 22–37.
[26] D. Thévenin, F. Behrendt, U. Maas, B. Przywara, J. Warnatz, Comput. Fluids 25 (1996) 485–496.
[27] R. Kee, J. Miller, T. Jefferson, Sandia National Laboratories Report SAND 80-8003, 1980.
[28] R. Kee, J. Warnatz, J. Miller, Sandia National Laboratories Report, SAND83-8209, 1983.
[29] A. Ern, V. Giovangigli, eglib server and user's manual, 2009.

[30] F. Williams, Combustion Theory, second ed., Addison-Wesley, USA, 1985.
[31] K. Kuo, Principles of Combustion, John Wesley & Sons Inc., 2005.
[32] V. Giovangigli, Multicomponent Flow Modeling, Birkhäuser, Boston, 1999.
[33] P.M.A. Honein, J. Comput. Phys. 201 (2004) 531–545.
[34] P.M.H. Choi, J. Comput. Phys. 11 (1994) 1–4.
[35] M. Baum, T. Poinsot, D. Thévenin, J. Comput. Phys. 116 (1994) 247–261.
[36] J. Warnatz, U. Maas, R.W. Dibble, Springer-Verlag, New York, 1996.
[37] U. Maas, J. Warnatz, Impact Comput. Sci. Eng. (1989) 394–420.
[38] D. Rosner, Transport Processes in Chemically Reacting Flow Systems, Dover, New York, 2000.
[39] J.O. Hirschfelder, C.F. Curtiss, Proc. Comb. Inst. 3 (1949) 121–127.
[40] R.J. Kee, M.E. Coltrin, P. Glarborg, Chemically Reacting Flow, Wiley Interscience, 2003.
[41] T. Poinsot, S.K. Lele, J. Comput. Phys. 101 (1992) 104–129.
[42] M.D. Smooke, V. Giovangigli, in: M.D. Smooke (Ed.), Reduced Kinetic Mechanism and Asymptotic Approximations for Methane-Air Flames, Lecture Notes in Physics, vol. 384, Springer-Verlag, 1991, pp. 1–47.
[43] S. Candel, D. Durox, S. Ducruix, A. Birbaud, N. Noiray, T. Schuller, Int. J. Aeroacoust. 8 (2009) 1–56.
[44] A.S. Al-Shahrany, D. Bradley, M. Lawes, K. Liu, R. Woolley, Combust. Sci. Techn. 178 (2006) 1771–1802.
[45] B. Cuenot, T. Poinsot, Combust. Flame 104 (1996) 11–137.
[46] T. Poinsot, D. Veynante, Theoretical and Numerical Combustion, 2nd ed., EdwardsRT Inc., Philadelphia, 2005.
[47] N.R. Edwards, A.C. Mcintosh, J. Brindley. Combust. Sci. Techn. 99 (1994) 179–199.